AIP | The Journal of
Chemical Physics

Kinetic measurements of the C2H5O2 radical using time-resolved cavity ring-down spectroscopy with a continuous source

Dmitry Melnik and Terry A. Miller

Citation: J. Chem. Phys. **139**, 094201 (2013); doi: 10.1063/1.4819474
View online: http://dx.doi.org/10.1063/1.4819474
View Table of Contents: http://jcp.aip.org/resource/1/JCPSA6/v139/i9
Published by the AIP Publishing LLC.

THE JOURNAL OF CHEMICAL PHYSICS **139**, 094201 (2013)

Kinetic measurements of the $C_2H_5O_2$ radical using time-resolved cavity ring-down spectroscopy with a continuous source

Dmitry Melnik and Terry A. Miller[a)]
Department of Chemistry, The Ohio State University, 120 W. 18th Avenue, Columbus, Ohio 43210, USA

(Received 3 June 2013; accepted 14 August 2013; published online 5 September 2013)

We report on the design of a time-resolved, high duty-factor cavity ring-down apparatus utilizing a continuous laser and detail a technique for the accurate and precise measurement of effective reaction rate constants with it. This report complements an earlier paper concerning the measurement of the absolute absorption cross-sections, σ_P, of reactive intermediates. To demonstrate the performance of the new technique, we have measured the decay rate of ethyl peroxy radicals by monitoring the $\tilde{A} \leftarrow \tilde{X}$ origin band of the G-conformer of these species. A measured value $k_{obs}/\sigma_P = 1.827(45) \times 10^7$ cm/s was determined and it, along with the previously measured value of σ_P, was used to derive the value of $k_{obs} = 9.66(44)\times10^{-14}$ cm^3/s, for the effective rate constant for ethyl peroxy self-reaction (all uncertainties are 1 σ). The present value of k_{obs} is compared to those previously reported, and sources of systematic errors and their impact are discussed. *© 2013 AIP Publishing LLC*. [http://dx.doi.org/10.1063/1.4819474]

I. INTRODUCTION

Organic peroxy radicals, RO_2 are important reactive intermediates in gas phase oxidation processes taking place in the lower atmosphere and combustion environments.[1–5] In the troposphere, they are involved in ozone production,[4,6,7] formation of photochemical smog and acid rain.[8–11] In low temperature combustion, peroxy radicals are involved in the chain-branching sequence of reactions that are necessary for the sustained combustion process,[12–14] and in processes interdicting soot formation.[15] It has been shown[1] that the thermodynamic properties of peroxy radicals result in the apparent negative temperature coefficient of the reaction rate in parts of the low temperature region. The isomerization of peroxy radicals may lead to autoignition and engine knock which have an adverse effect on the efficiency of internal combustion engines and fuel economy.[13,14] For a better quantitative understanding and managing of the oxidation processes in both atmospheric and combustion environments it is necessary to obtain accurate information about peroxy radical chemical properties, of which the reaction rate coefficients (RRCs), are among the most important.

In environments such as the troposphere or an internal combustion engine, peroxy radicals react with a number of species,[2,4,5,16,17] such as NO, NO_2, O_3, and themselves. The latter group of reactions can be divided into two categories, peroxy radicals self-reactions, $RO_2 + RO_2$, and reactions between different peroxy radical species, $RO_2 + R'O_2$ ($R \neq R'$), including an important category of reactions $RO_2 + HO_2$. The self-reaction of a number of RO_2 species has been extensively studied in the past. It has been concluded that for most radical species the observed reactant decay follows a simple second order kinetic law[2,4] with the observed RRC, k_{obs}, accounting for the decay rate of the reactants in the primary elementary processes as well as the secondary chemistry effects. Traditionally, the values of k_{obs} were obtained by observation of the decay of the radical number density by monitoring the absorption signal at the peak absorption frequency of the $\tilde{B} \leftarrow \tilde{X}$ electronic transition in the UV region. Despite a relatively simple chemical mechanism of the peroxy radical self-reaction as well as large peak absorption cross-section of the $\tilde{B} \leftarrow \tilde{X}$ transition,[2] the experimental values of the self-reaction RRCs typically suffer experimental uncertainties of 15%–25% and substantially vary between reports of different research groups (for example, within as much as factor of three[2,4,18–26] for ethyl peroxy radical).

Additional complications arise in the measurement of the RRC of the reactions between different radical species. First, due to extreme similarity[7] of the $\tilde{B} \leftarrow \tilde{X}$ absorption spectra of organic peroxy radicals, the measured time dependent absorption signal often gives the total number density of all present peroxy radicals plus, possibly, a number of other interfering species,[11] rather than that of just the desired peroxy radicals. Second, as additional reactive species are introduced to the media, the time dependence of the concentrations of an individual species becomes more complicated.[11,27] The analysis of such experimental data requires either using complex mathematical models, or deconvolution of decay profiles obtained at different frequencies for strongly overlapping spectra.[28] Third, a rapidly growing number of elementary chemical processes whose individual RRC are poorly determined, results in rather poor quantitative understanding of the overall chemical process.[11,27,28]

In the past decade, substantial progress has been made in the investigation of the weak $\tilde{A} \leftarrow \tilde{X}$ electronic transition[29–34] of organic peroxy radicals in the NIR region in the vicinity of 1.3 μm. Since the $\tilde{A}$ electronic state is bound, the $\tilde{A} \leftarrow \tilde{X}$ spectra exhibit unique structure that identifies the chemical and geometric structure of the carrier.[31,32,35] On the other hand, its relatively small (of the order of

---

[a)] tamiller@chemistry.ohio-state.edu

10^{-21}–10^{-20} cm^2) absorption cross-section[30,31,33,36,37] did not allow for its use as analytical tool until the advent of sensitive experimental techniques such as cavity ring-down spectroscopy (CRDS).[38]

For the purpose of kinetic studies, the CRDS monitoring of the NIR $\tilde{A} \leftarrow \tilde{X}$ absorption offers two major benefits. First, the structure of the NIR absorption spectra provides chemical species-specific detection, allowing one to distinguish among different isomers and conformers of the selected radical and thereby permitting one to selectively monitor their temporal decay profiles. Additionally, the NIR region is relatively weakly congested by spectra of radical precursors and products of the chemical reactions involved, which however, do often absorb in the UV region thus complicating the analysis of the kinetic data.[27,39] Since the absorption signal obtained from the analysis of the ringdown decays is insensitive to the power fluctuations of the light source this technique generally allows for more accurate determination of the absorption losses and therefore can produce a more accurate and precise kinetic decay curve.

The CRDS-based kinetic studies of different reactive species have been reported previously.[26,27,41,42] In the experimental studies by Atkinson and Hudgens[26] and Atkinson and Spillman[37] the reactive species were produced by laser photolysis. The kinetic decay of the species of interest has been obtained by measuring the absorption at a single delay time after the photolysis pulse. The decay curve is reconstructed from a succession of measurements with different values of photolysis-to-probe delay. This technique, while easy to implement, suffers from a low duty factor. Additionally, since every data point is obtained with a different sample of the reactive species, this technique is vulnerable to pulse to pulse fluctuations of the initial radical concentration, e.g., due to photolysis laser power fluctuations. A more advanced version of time-resolved kinetic measurements has been implemented by Fittschen and co-workers,[40,41] in which a series of measurements of the absorption in the reaction region were made following a single event synthesis of the reactive species (HO$_2$), i.e., by observation of the evolution of the same sample of radicals. In these studies, however, the authors pursued determination of the absorption cross-section, and combined their observed temporal decay profiles and the recommended kinetic decay rate of self-reaction of HO$_2$ to obtain the concentration of radicals. Additionally, a number of factors, such as low laser power and the necessity to sweep the cavity length over the entire free spectrum range due to lack cavity length stabilisation,[41] prevented the authors from achieving high enough values of the duty factor to follow a single kinetic event in detail.

In case of a well established reaction mechanism resulting in a simple decay law, which is the case[42,43] for HO$_2$ and reasonably high signal-to-noise ratio of the ringdown signal, a small data set is sufficient to obtain accurate results. However, in more complicated cases, such as measuring cross-reaction rates with complex reaction mechanisms, a large number of elementary processes[27,28,39] and potential deviations from a simple power decay law,[39,44] measurement of the kinetic decay with high temporal resolution becomes critical for the accurate determination of the relevant RRCs and improvement of our understanding of the mechanism of the reaction of interest.

In the present work we will discuss the development of a high duty factor CW-CRDS apparatus for the measurement of the kinetic decay of individual samples of reactive species. To demonstrate its capabilities, we report the measurement of the effective RRC for the self-reaction of ethyl peroxy radicals k_{obs} obtained by monitoring the absorption decay at the peak of the $\tilde{A} \leftarrow \tilde{X}$ transition of the G-conformer[31,33] of this radical. We will also discuss possible sources of errors (Appendix A) and evaluate the capabilities of this technique in terms of the range of the RRCs that can be successfully measured (Appendix B).

II. OVERVIEW OF THE KINETICS AND CONCENTRATION DETERMINATION OF C$_2$H$_5$O$_2$

A. Concentration profile of the reactive species as a function of time

In a clean laboratory environment,[31,33,45] peroxy radicals, such as C$_2$H$_5$O$_2$ are synthesized by photolytic generation of alkyl (e.g., ethyl) radicals from the suitable precursor (e.g., 3-pentanone) followed by rapid addition of molecular oxygen. Under conditions of a large stationary uniform sample, in the absence of other reaction partners, ethyl peroxy radicals are chemically removed from the reaction region by self-reaction. The mechanism of this reaction can be represented by a set of the elementary processes[33]

$$C_2H_5COC_2H_5 \xrightarrow{193\ nm} CO + 2C_2H_5, \tag{1a}$$

$$C_2H_5 + O_2 \rightarrow C_2H_5O_2, \quad 2.7\times10^{-12}, \tag{1b}$$

$$C_2H_5 + C_2H_5 \rightarrow C_4H_{10}, \quad 2.0\times10^{-11}, \tag{1c}$$

$$C_2H_5O_2 + C_2H_5O_2 \rightarrow 2C_2H_5O + O_2, \quad 4.2\times10^{-14}, \tag{1d}$$

$$C_2H_5O_2 + C_2H_5O_2 \rightarrow CH_3CHO + C_2H_5OH + O_2, \quad 2.4\times10^{-14}, \tag{1e}$$

$$C_2H_5O + O_2 \rightarrow CH_3CHO + HO_2, \quad 9.5\times10^{-15}, \tag{1f}$$

$$C_2H_5O_2 + HO_2 \rightarrow C_2H_5OOH + O_2, \quad 7.7\times10^{-12}, \tag{1g}$$

$$HO_2 + HO_2 \rightarrow H_2O_2 + O_2, \quad 1.6\times10^{-12}, \tag{1h}$$

$$HO_2 + HO_2 + N_2 \rightarrow H_2O_2 + N_2, \quad 5.2\times10^{-32}\cdot N_{N_2}, \tag{1i}$$

$$HO_2 + HO_2 + O_2 \rightarrow H_2O_2 + O_2, \quad 4.5\times10^{-32}\cdot N_{O_2}, \tag{1j}$$

$$C_2H_5O + C_2H_5O_2 \rightarrow C_2H_5OOH + CH_3CHO, \quad 1.7\times10^{-11}, \tag{1k}$$

$$C_2H_5O + HO_2 \rightarrow C_2H_5OH + O_2, \quad 1.6\times10^{-11}. \tag{1l}$$

The values of the rate constants (in cm^3/s) of Eqs. (1b) and (1c) are taken from the paper by Atkinson and Hudgens,[26] rate constants, Eqs. (1d) and (1e), are obtained from the review by Lightfoot *et al.*,[2] and rate constants Eqs. (1f) and (1g) are taken from the review by Atkinson.[5] The rate constants for reactions $k_{1h} - k_{1j}$ are obtained from the IUPAC database. The value of the rate constant k_{1k} is obtained from the work[25] of Noell *et al.*, and the value of k_{1l} is taken from the report[22] of Anastasi *et al.* At high concentrations of oxygen, such as those found at the experimental conditions used in the present studies, the rate of reaction, Eq. (1b), far exceeds that of the competing reaction, Eq. (1c), ensuring essentially stoichiometric conversion of ethyl to ethyl peroxy radicals.

The primary removal of the ethyl peroxy radicals occurs through the steps given in Eqs. (1d) and (1e). The latter of these two reactions results in formation of stable products. In the former reaction, one ethoxy molecule is produced per one ethyl peroxy reactant. Due to high concentrations of oxygen, ethoxy radicals are rapidly converted to HO_2 through the step in Eq. (1f) with subsequent removal of additional ethyl peroxy radicals through step Eq. (1g). The high rate of reactivity of HO_2 with ethyl peroxy, as well as its low concentration under typical conditions ensures that the steps, Eqs. (1h)–(1j), do not significantly affect the overall process. For similar reasons, the effect of the reactions, Eqs. (1k) and (1l), is also negligible. Hence, each occurrence of reaction, Eq. (1d), results in the loss of two additional peroxy radicals (four in total), whereas only two peroxy radicals are destroyed in the path of Eq. (1e). Thus the total rate of removal of peroxy radicals, $k_{obs} = 2k_{1d} + k_{1e}$ must be distinguished from the RRC, $k_{1d} + k_{1e}$, of the primary reaction. The two rates, primary and observed, can be related to one another by the introduction of the branching ratio, α, indicating the fraction of the elementary reactions of ethyl peroxy radicals with themselves proceeding along the path of Eq. (1d):

$$k_{obs} = (k_{1d} + k_{1e})(1 + \alpha), \tag{2a}$$

$$\alpha = \frac{k_{1d}}{k_{1d} + k_{1e}}. \tag{2b}$$

In the absence of other removal mechanisms apart from the self-reaction, the evolution of the concentration of ethyl peroxy radicals follows the simple second-order kinetic decay law,

$$\frac{\partial N(x,t)}{\partial t} = -2k_{obs}N(x,t)^2, \tag{3}$$

whose solution is well known and is given by

$$N(x,t)^{-1} = N(x,0)^{-1} + 2k_{obs}t \tag{4}$$

in which $N(x, t)$ is the concentration of the reactant species at point x and time t. The relationship between k_{obs} and the RRCs of the elementary reactions k_{1d} and k_{1e} given by Eq. (2) is based on the approximation that the secondary processes, Eqs. (1f) and (1g), result in rapid stoichiometric removal of additional ethyl peroxy radical. A convenient summary of the history of the previously reported values of α is provided by Ref. 25. As is shown there, α values have been reported that range from more than 0.7 to slightly less than 0.3. For this reason we have compared the results for the complete reaction mechanism, Eq. (1), with the simplified results, Eqs. (2)–(4), with the value of k_{obs} determined from Eq. (2) and the values of k_{1d} and k_{1e} given in Eq. (1). These values correspond to $\alpha = 0.64$ which is consistent with the value of 0.62(10) recommended by Atkinson.[5] These calculations, performed for the initial concentration of C_2H_5 radicals at 2×10^{15} cm^{-3} are illustrated in Fig. 1. The concentration profiles are plotted with 10 μs time resolution. Two nearly superimposed curves, red and black, show the kinetic decay of ethyl peroxy radicals given by Eq. (4), and obtained from the numerical solution of the system of kinetic equations for the complete mechanism in Eq. (1), respectively. The dashed brown curve shows the difference between these two predicted kinetic decay profiles multiplied by a factor of 300. As Fig. 1 shows the difference between the complete mechanism and the simplified model is considerably less than 1%. For comparison, we have re-run these calculations using the most recently reported values[25] of $\alpha = 0.28$ and $k_{obs} = 1.20 \times 10^{-13}$ cm^3/s, and the values of k_{1d} and k_{1e} derived using Eq. (2). Although not shown in Fig. 1, the difference between full and effective mechanisms in the latter calculations is also substantially below 1%. We conclude that under the condition of the experiment the effective simple second-order decay law for the ethyl peroxy radicals accurately represents the full reaction mechanism within a wide range of α values. Further discussion of the details of the full mechanism and their implications for the value of k_{obs} is given in Appendix A. Although not a subject of this paper, the evolution of the concentrations of C_2H_5O (blue curve) and HO_2 (green curve), both multiplied by a factor of 100 are also shown in Fig. 1. Hence the concentrations of HO_2 and C_2H_5O

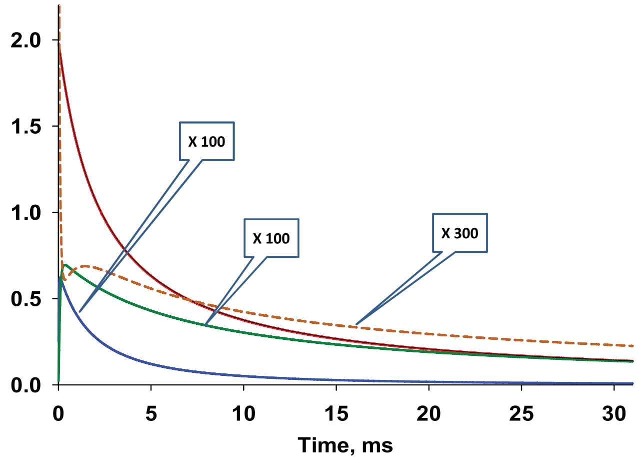

FIG. 1. Simulated evolution of the concentration of the reactants and intermediates of the self-reaction of $C_2H_5O_2$. The superimposed red and black curve are time-dependent concentrations of $C_2H_5O_2$ calculated using the rigorous mathematical model representing the reaction mechanism in Eq. (1) (black curve) and the approximation of Eq. (4). Their difference, multiplied by a factor of 300, is given by the brown dashed curve. The concentrations of the C_2H_5O, and HO_2 radicals, multiplied by 100, are shown in blue and green traces, respectively.

are lower than that of the ethyl peroxy by at least two orders of magnitude at all times during the decay process.

In a realistic laboratory experiment, reactive species are also subject to non-chemical removal mechanisms, such as displacement from the detection zone by diffusion or macroscopic flow. For an accurate determination of the k_{obs}, such processes need to be properly accounted for. To do that we introduce the assumption, which will be examined in Appendix A, that the experiments are conducted under conditions of slow laminar flow and any effects of turbulence can be ignored. Under such conditions, the number density of the reactive species in the reactive sample can be described by the Smoluchowski equation,[46]

$$\frac{\partial N(x,t)}{\partial t} = \nabla\cdot(D\nabla N(x,t)) - \nabla\cdot(\overrightarrow{v}N(x,t)) - 2k_{obs}N(x,t)^2, \tag{5}$$

where D is the diffusion constant, v is the macroscopic velocity of the sample and the last term accounts for the chemical removal of the species. In case of steady one-dimensional flow of an incompressible medium (i.e., $N(x,t)\nabla\cdot v = 0$), such as a gas at low speeds and a spatially invariant D, Eq. (5) reduces to

$$\frac{\partial N(x,t)}{\partial t} = D\nabla^2 N(x,t) - \overrightarrow{v}\cdot\nabla N(x,t) - 2k_{obs}N(x,t)^2. \tag{6}$$

The general solution of Eq. (6) with realistic boundary conditions is rather complex and is outside of the scope of this work. To use this equation for the numerical analysis of the experimental data, we introduce two simplifications. First we note that in the present work the reaction cell is configured such that the extended sample is generated by the transverse illumination of the cell by a near-uniform, masked photolysis laser beam (see details in Sec. III), and removed by pumping along the cell axis, coincident with the path of the probe beam. In such a configuration, the gradient of the radical concentration is perpendicular to the macroscopic velocity at all points along the sample axis except for relatively small regions at the ends of the sample, therefore the second term in Eq. (6) essentially vanishes.

Second, we note that the removal of radicals from the probe region due to diffusion depends on the distribution function of the radical density in the direction perpendicular to the probe beam. This distribution function changes with time due to the chemical reaction and therefore the rate of radical removal due to the first (diffusion) term in Eq. (6) is also time-dependent. In general, this removal rate increases with the absolute concentration of the radicals. Therefore, as the second simplification we assume that the removal rate due to the diffusion is proportional to the radical concentration along the axis of the sample and replace the first term on the right-hand side of Eq. (6) with the first-order kinetic term,

$$\frac{\partial N(x,t)}{\partial t} = -k_1 N(x,t) - 2k_{obs}N(x,t)^2, \tag{7}$$

where the first-order constant, k_1, accounts for all physical removal processes of the radicals from the near-axis region of the sample. In Appendix A we will discuss the implication of this assumption and evaluate the systematic error resulting from such a simplification. The minus sign in front of k_1 is introduced such that k_1 has a positive value. The closed form solution of Eq. (7) can be obtained either analytically or using contemporary computational software such as Mathematica, and is given as

$$N(x,t) = \frac{k_1 N(x,0)}{k_1 e^{k_1 t} - 2k_{obs}N(x,0) + 2k_{obs}e^{k_1 t}N(x,0)}, \tag{8}$$

where $N(x, 0)$ is the initial concentration of radicals. In the limit of $k_1 \to 0$, Eq. (8) reduces to Eq. (4), which can be verified directly by expanding the exponentials in the denominator in a power series through the linear term.

B. Kinetic model

To make use of Eq. (8) we need to recast it in terms of the experimentally measured quantities. Spectroscopic determination of k_{obs} involves the observation of the time evolution of the light absorption, $A(t)$, in a finite sample of the generally variable length, $L(t)$, (see Sec. III for details) due to the processes of chemical and physical removal described above. Using Beer's law for optically thin sample, the time-dependent absorption can be written as

$$A(t) \equiv \frac{\Delta I(t)}{I_0(t)} = \sigma_P \int_0^{L(t)} N(t,x)dx, \tag{9}$$

where I_0 is the intensity of the incident radiation, ΔI is the intensity loss due to the absorption in the sample, x is the coordinate along the line of sight, and σ_P is the absorption cross-section. Combining Eq. (8) with Eq. (9) and performing the integration, we obtain the expression for the time evolution of the absorption signal $A(t)$,

$$A(t) = \frac{\sigma_P k_1 N_0 (L_0 - vt)}{k_1 e^{k_1 t} - 2k_{obs}N_0 + 2k_{obs}e^{k_1 t}N_0}, \tag{10a}$$

$$N_0 = \frac{1}{L_0}\int_0^{L_0} N(x,0)dx, \tag{10b}$$

where $L_0 = L(t = 0)$ and the initial distribution of species $N(x, 0)$ is assumed to be independent of x. Effects of the sample nonuniformity along the x coordinate will be discussed in Appendix A.

In the discussion above we made an assumption that experimental conditions are chosen such that the chemical reaction is the dominant process of the removal of the ethyl peroxy radicals. Alternatively, the time interval for the analysis of the kinetic data needs to be chosen such that chemical removal rate is much greater than the removal rate due to non-chemical processes at all times,

$$k_1 N(t) \ll 2k_{obs}N^2(t), \tag{11}$$

where we explicitly removed the x-dependence of radicals concentration in the sample. Using Eq. (4), we obtain

$$t \ll \frac{2k_{obs}N_0 - k_1}{2N_0 k_{obs} k_1}. \tag{12}$$

Since at $t = 0$ the chemical removal is dominant, we can ignore the second term in the numerator in Eq. (12) and obtain

$$k_1 t \ll 1. \tag{13}$$

Using this criterion and expanding exponentials in Eq. (10a), we obtain for $A(t)$ at times limited by Eq. (13),

$$A(t) = \frac{A_0\left[1 - \dfrac{v}{L_0}t\right]}{1 + \left[k_1 + 2\left(\dfrac{k_{obs}}{\sigma_P}\right)\dfrac{A_0}{L_0}\right]t}, \tag{14}$$

where A_0 is the absorption at the beginning of the monitoring, $A(t = 0)$. Eqution (14) shows that the rate constant k_1 adds to the absorption decay rate, and even though relatively small in magnitude, it can lead to an overestimation of k_{obs}/σ_P by approximately $k_1L_0/(2A_0)$ if not properly accounted for. Additionally, the flow velocity must be known from an independent measurement to avoid systematic errors associated with macroscopic removal of the species. Both of these parameters, in principle, can be measured by monitoring the absorption decay of an inert species, for which the RRC, k_{obs}, is negligible and for which Eq. (10) reduces to

$$A(t) = A_0\left[1 - \frac{v}{L_0}t\right]e^{-k_1 t}. \tag{15}$$

Under realistic experimental conditions of a near-static sample, k_1 and v are difficult to obtain independently due to high degree of correlation between these parameters arising in the nonlinear fit of the experimental data to Eq. (15). This can be illustrated by expanding Eq. (15) to the first order term (at times limited by Eq. (13)), which gives

$$A(t) = A_0\left[1 - \frac{1}{L_0}(v + k_1L_0)\,t\right], \tag{16}$$

i.e., only the sum of v and k_1L_0 can be experimentally measured by monitoring of absorption of the chemically inert species over the time interval relevant to the kinetic measurements. The value in parentheses in Eq. (16) has dimension of velocity and at low values of k_1 becomes equal to the physical flow rate of the sample v. Therefore, we introduce the “effective” flow rate,

$$u = v + k_1L_0, \tag{17}$$

which takes into account all physical removal processes to the given level of approximation.

To utilize flow rate data for an inert species in the analysis of the absorption decay of the reactive species, we need to modify Eq. (14). To do so, we note that the term k_1t in the denominator remains small compared to the rest of the denominator at all times during the measurement. Therefore, we rewrite Eq. (14) as

$$A(t) \approx \frac{A_0\left[1 - \dfrac{v}{L_0}t\right]}{\left[1 + 2\left(\dfrac{k_{obs}}{\sigma_P}\right)\dfrac{A_0}{L_0}t\right](1 + k_1t)} = \frac{A_0\left[1 - \dfrac{u}{L_0}t\right]}{\left[1 + 2\left(\dfrac{k_{obs}}{\sigma_P}\right)\dfrac{A_0}{L_0}t\right]}, \tag{18}$$

where small terms quadratic in time are ignored.

Absorption decay curves simulated for $L_0 = 5$ cm, $v = 3$ cm/s, $k_1 = 2\ \mathrm{s}^{-1}$ (resulting in $u = 13$ cm/s), $k_{obs}/\sigma_P = 2 \times 10^7$ cm/s are shown in Fig. 2(a). Two nearly superimposed curves, black and red, show the evolution of the absorption of peroxy radicals calculated using Eqs. (10a) and (18), respectively. The blue curve shows the difference between these decay profiles, multiplied by a factor of 100. These simulations illustrate that the simplified model, Eq. (18), gives an error no greater than 0.15 ppm which falls below the noise level of the absorption signal in our experiments. Fig. 2(b) shows similar predictions for the absorption profiles of the inert species at $A_0 = 20$ ppm and the same values of v, k_1, and L_0 as those being used to generated the traces in Fig. 2(a). These simulations show that the use of the simplified model, Eq. (16), in lieu of the rigorous model, Eq. (15), produces qualitatively similar results on the time scale of measurements but introduces about a 10% overestimate of the value of u. Therefore, Eq. (16) and the second equality in Eq. (18) were used for the analysis of the experimental data in this work and we examine the effects of such overestimates in Appendix A.

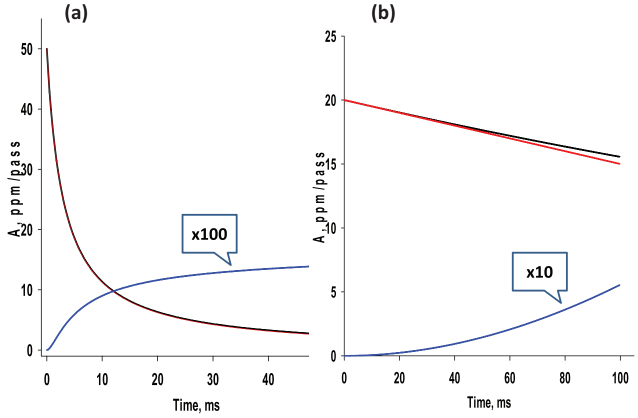

FIG. 2. Simulations of the absorption decay, calculated using the rigorous (black curves) and approximate (red curves) expressions. The differences between the rigorous and approximate models, multiplied by numerical factors as shown, are given by the blue curves. Panel (a) shows the simulation for the absorption decays of the ethyl peroxy radicals. Panel (b) shows simulation for the chemically inert molecules. See text for the details and conditions of the simulations.

C. Absorption profiles measurement via CRDS

Equation (14) shows that the quantity $(\frac{k_{obs}}{\sigma_P})$ is directly measured in the actual experiment rather than k_{obs} itself. Therefore, the absorption cross-section σ_P needs to be known to adequate accuracy since its uncertainty defines a lower limit in the uncertainty of k_{obs} derived from such a measurement.

The $\tilde{A} \leftarrow \tilde{X}$ transition of ethyl peroxy is located in the NIR region which makes it convenient for the quantitative measurement via the CRDS technique. Previously,[31] the spectra of the two ethyl peroxy conformers, T and G were reported under ambient conditions, and subsequently,[33] the peak absorption cross-section, σ_P, for the spectrum feature at 7596 cm^{-1} corresponding to the peak of the R-branch of the origin of $\tilde{A} \leftarrow \tilde{X}$ electronic transition, was experimentally measured.

Under the conditions of the present and previously reported[31,33] measurements, this feature is relatively broad and lacks fine spectrum details.[31,34] A sufficient width of the absorption feature is important in two respects. First, in order to make a quantitatively accurate measure of the absorption, the absorption peak must be wide compared to the laser bandwidth.[38,47] If such conditions are achieved, the experimentally obtained value of the fractional absorption is insensitive to the laser bandwidth and therefore absorption measurements done with a pulsed multimode laser (such as a Stokes-shifted dye laser) used in measurements of the σ_P, and a narrow band single-mode diode laser will provide identical results. Second, the use of a broad absorption feature eliminates the need of locking the laser to, or scanning over,[40,41] a narrow spectral range in the vicinity of the peak absorption, thus greatly simplifying and speeding up the data acquisition protocol.

The nature of the CRDS protocol limits the time resolution of the measurements. A single value of $A(t)$ is derived from the analysis of an individual ring-down decay curve over a time period of 3-5 ring-down times, which is of the order of 200–300 μs. The speed of the chemical decay process can be characterized by a half-life time, $\tau_{1/2}$, defined as time measured since the start of the kinetic data acquisition at which the concentration of the reactive species is reduced by a factor of two. Assuming that the chemical removal process is dominant and the radicals are evenly distributed over the sample at $t = 0$, we obtain

$$\tau_{1/2} = (2k_{obs}N_0)^{-1}\,. \tag{19}$$

The half-life time $\tau_{1/2}$ defines the time scale of the kinetic experiment. For the accurate measurement of the RRC, two criteria must be met. First, the time resolution Δt must be small compared to $\tau_{1/2}$. Second, the time span, T_m, over which the kinetic decay is observed must be large compared to $\tau_{1/2}$. Using an order-of-magnitude argument, we define the practical limits for Δt and T_m,

$$\Delta t \le 0.1 \cdot \tau_{1/2} = (20k_{obs}N_0)^{-1}\,, \tag{20a}$$

$$T_m \ge 10\tau_{1/2}. \tag{20b}$$

For the values of RRCs in Eq. (1) and the experimental conditions,[33] the value of $\tau_{1/2}$ is ≈2.5 ms, hence a time resolution of ≈250 μs and recording time for measuring kinetic decay of ≈25 ms is required to obtain data to accurately determine the RRC for self-reaction of the ethyl peroxy radicals.

III. EXPERIMENTAL

A. Instrumental design

A schematic diagram of the experimental setup is given in Fig. 3. We used one of the arms (arm A) of the previously described[33] dual wavelength CRDS apparatus to build the CW-CRDS system, with arm B being reserved for future extensions of the experiment. The optical train for the photolysis laser beam is shown in Fig. 4. A rectangular reaction cell with cross section 12.5 mm × 25 mm is inserted in the middle of the 70-cm long CRDS cavity and is furnished with quartz windows allowing the radiation from the photolysis laser to define a zone for the reactive species. The beam of the excimer laser entering the cell is reshaped by cylindrical and spherical lenses and restricted by the mask placed 20 cm away from the axis of the cell, resulting in formation of the reaction zone whose dimensions are 8 mm high and 60 mm long in the plane containing the probe beam and perpendicular to the excimer beam. The precursor mixture is introduced into the cell through two input ports located at either side of the reaction region, 175 mm apart. The cell is evacuated through a single port located above the center of the photolysis window by an Alcatel 2012AC vacuum pump interfaced through a needle valve to control the flow rate.

The radiation of an external cavity diode laser (ECDL, New Focus Velocity TLB-6324) is coupled to the TEM_{00} mode of CRDS cavity through one of the mirrors (Los Gatos Research, 99.995% minimum reflectivity) using mode-matching optics (MMO). To prevent back-reflection of the radiation to the laser diode, two 30-dB optical isolators (OI) were placed after the exit aperture of the laser. The laser

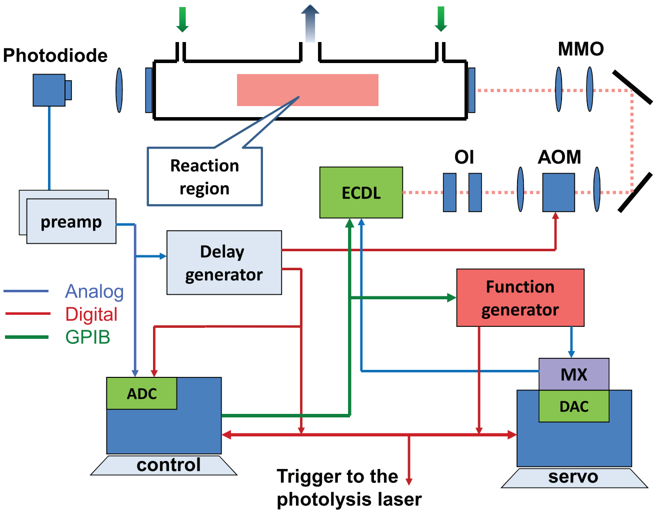

FIG. 3. Schematic diagram of the experimental setup. Abbreviations: ECDL - external cavity diode laser, OI - optical isolators, AOM - acousto-optical modulator, MMO - mode-matching optics. See text for more detail.

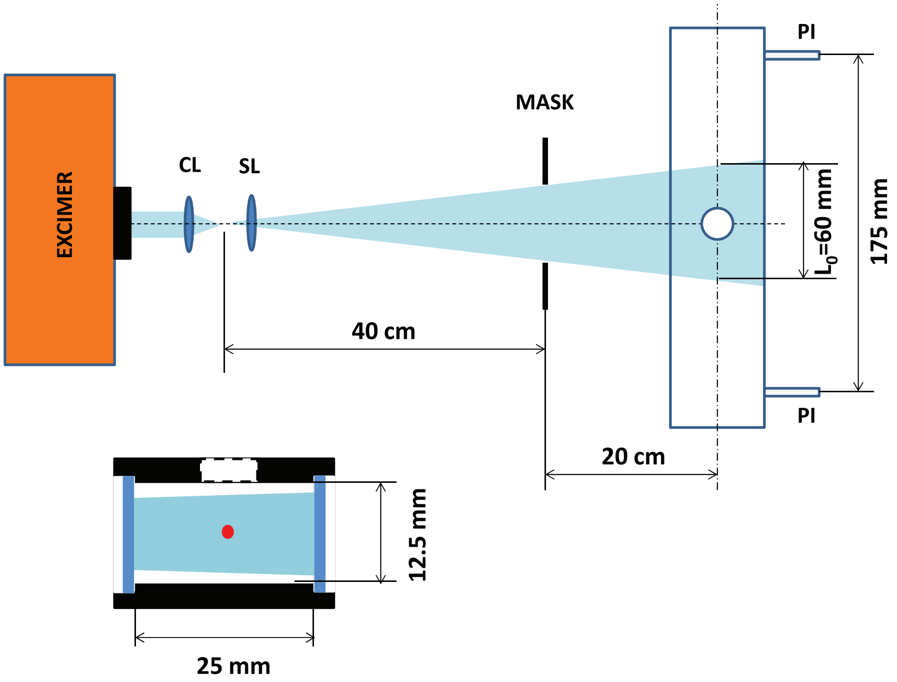

FIG. 4. Schematic diagram of the optical train for the photolysis beam. Abbreviations: CL - cylindrical lens, SL - spherical lens, PI - precursor inlet. The pump port location is shown as white circle in the middle of the cell. The inset below shows the cross-section of the reaction cell in the plane perpendicular to the probe beam. The position of probe beam (waist diameter 1.4 mm) is marked by a red dot. See text for more details.

radiation can be rapidly coupled and de-coupled from the cavity using an acousto-optic modulator (AOM, Brimrose Corporation, IPM-80-13) capable of transmitting over 70% of radiation into the first order diffracted beam. To maintain single mode operation of the laser, typical output power within the range of 4.5–5.5 mW was used, resulting in about 3 mW impinging upon the mirror of the CRDS cavity.

The CRDS signal is captured by a photodiode (Thorlabs, PDA10CS) and amplified by two consecutive custom made preamplifiers. To reduce electrical noises and avoid ground loops in low signal circuits, the built-in preamplifier of the photodiode and the first stage custom made preamplifier are battery powered. The output of the second stage preamplifier is recorded by the data acquisition board (ADC, Measurement Computing, PCI-4020/12). The same signal is interfaced to a digital delay generator (Stanford Research Systems, DG535) to provide a trigger signal for the AOM and a reference signal for timing circuits. The resulting digital output from the delay generator is also recorded by the ADC to facilitate the data processing.

In the present version of the spectrometer, the laser frequency dithers around a given CRDS cavity resonance using a feedback circuit. To accomplish this, we used an arbitrary function generator (Agilent, model 33220A) to drive the PZT actuator of the ECDL with a periodic sawtooth signal. The analog output of the function generator is added to the signal generated by the DAC (Access, PCI-DA12-6) installed in the dedicated servo computer, through a custom-made analog mixing circuit (MX). The output of the MX is supplied to the EDCL. The real time software run by the servo computer responds to the digital signals provided by the delay generator and function generator, and controlled through the custom made parallel port link by the control computer running data acquisition software. Time-insensitive operation settings of the function generator and EDCL are monitored through the GPIB interface by the control computer.

B. Data acquisition protocol

The choice of the experimental protocol is defined by the requirements imposed by the kinetic mechanism, spectroscopic properties of the radicals, and instrumental specifics. Since the bandwidth of the CW ECDL laser (<1 MHz) is much narrower than either that of the Raman-shifted pulsed dye laser (1–3 GHz) which was used[33] for measurements of σ_P, or the separation between the CRDS cavity modes (210.8 MHz), the CW-CRDS requires synchronization of the laser frequency and the frequency of the cavity resonance for a ring-down event to occur.

In general, an ECDL laser lacks the intrinsic capability to stabilize its frequency to sub-GHz accuracy and needs to be referenced to an external device or frequency marker. An example of such marker is a CRDS cavity resonance. CRDS resonance frequencies are not stable either, but "drift" due to the thermal variations in the environment of the CRDS cavity. A typical coefficient of linear thermal expansion for the cavity material (stainless steel) of about 10^{-5}/K implies that a mirror-to-mirror distance in a 70 cm long cavity varies up to 7 μm/K, or about 10 half-wavelength at the frequency of $\tilde{A} \leftarrow \tilde{X}$ origin transition of the ethyl peroxy. Viewed from a different perspective, the frequency variation of a particular cavity mode is of the order of 0.06 cm^{-1}/K. The width of the peak of the R-branch of the origin transition is of the order[31,33] of 1 cm^{-1}. Hence, an environment with

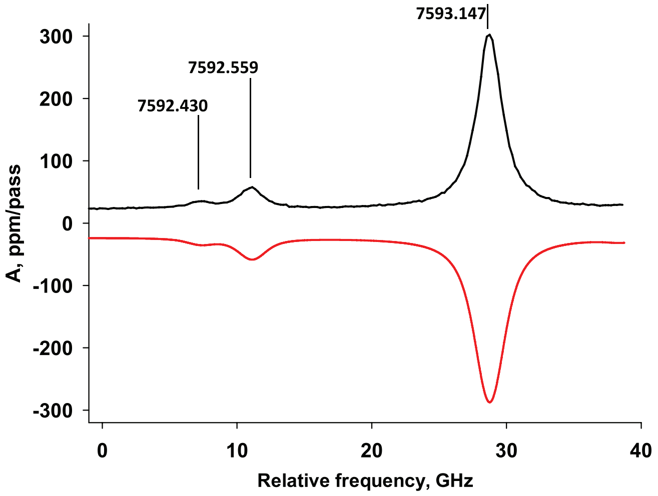

FIG. 5. Water absorption lines used for the frequency calibration of the diode laser. The top black trace shows the experimental trace obtained by a rapid, 420 GHz/s sweep over about 1 cm^{-1} in the vicinity of the peak absorption of the ethyl peroxy radicals. The bottom, inverted red trace, shows simulation of the absorption using the data from HITRAN database. The absolute transition frequencies from HITRAN (in cm^{-1}) are shown. The details of the plot simulation and transition assignment are given in the text.

temperature control of 1 K is sufficient to ensure overlap of the laser frequency with the spectral feature without sacrificing the accuracy of the absorption measurements.

The absolute frequency of the laser is calibrated by recording water absorption lines in the vicinity of the target frequency observed by substitution of the organic precursor with a 10% mixture of ambient air. Figure 5 shows the experimental trace (black) obtained during a rapid sweep of the laser frequency coupled to the CRDS cavity over a succession of the cavity TEM$_{00}$ resonances in the vicinity of the target frequency. Three water lines are observed, (021) 7_{53} ← (000) 6_{16} at 7592.430 cm^{-1}, (101) 7_{52} ← (000) 6_{33} at 7592.559 cm^{-1} and a stronger feature, (002) 4_{32} ← (000) 3_{21} at 7593.147 cm^{-1}. The bottom trace show the simulation of the absorption lines at T = 298 K, P = 300 Torr and optical path length $LN_{H_2O} = 6.9\times 10^{17}$ cm^{-2} using the data from the HITRAN database.[48]

A succession of the ring-down events is generated by dithering the laser frequency around a CRDS cavity resonance with repetition rate 1.8–2.0 kHz, resulting in a ring-down event twice a period, ensuring a temporal resolution of 250–270 μs. The dither rate is limited by two factors. First, the small amplitude dither signal supplied by a function generator is fed directly to the PZT of the ECDL, whose combined mechanical and electronic input bandwidth is limited at 2 kHz. Second, the consecutive ring-down events must be separated in time sufficiently so that each ring-down event is not initiated before the preceding event is essentially complete. In the present setup, a typical ringdown time in the cavity with organic precursor present, is $\tau_r = 60$–$80\ \mu$s, meaning that the time delay between the adjacent events is roughly $4\tau_r$, which also sets the limit of the dither rate at the present time. At these conditions, the chosen data acquisition protocol allows for near-continuous data acquisition during the chemical decay process.

The following, or “pseudo-locking,” of the laser frequency to the CRDS resonance is achieved by the implementation of a feedback circuit which includes the digital interface to the servo computer and real-time software analyzing the timing of the process. The frequency-following technique is illustrated in Fig. 6. The analog output of the arbitrary

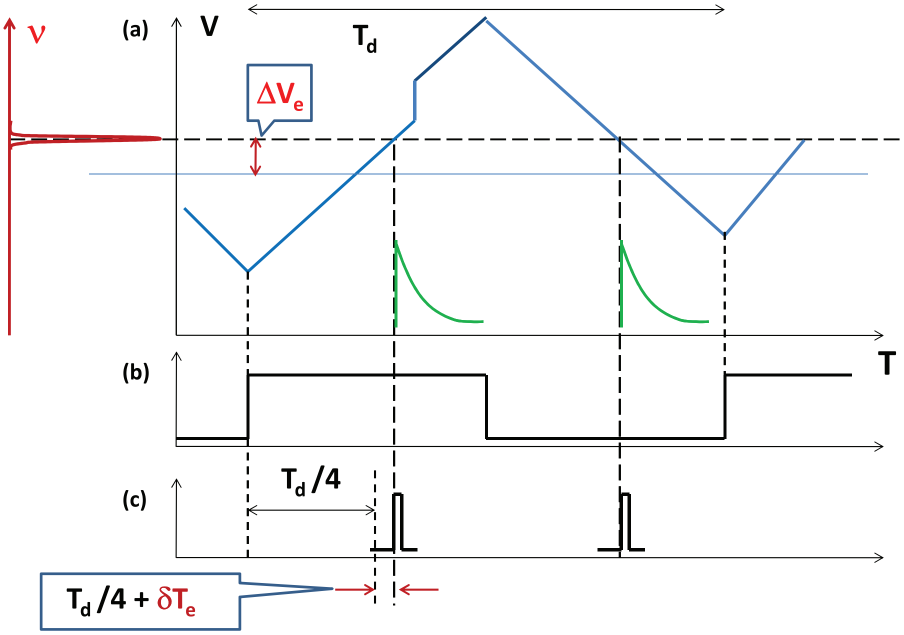

FIG. 6. The “following,” or “pseudo-locking” scheme. The laser frequency is dithered around the CRDS cavity resonance (red trace at the left) by applying a periodic sawtooth voltage (blue trace) to the diode laser PZT. The resulting periodic frequency sweep produces ring-down events (green traces) twice a period as the laser frequency matches the frequency of the cavity resonance, as shown in panel (a). A shift of the laser center frequency of the dither with respect to the cavity resonance is measured by the delay between function generator sync signal, panel (b), and digital signal produced by the ring-down event, panel (c). An analog error signal ΔV_e is generated to produce a compensating shift of the center dither frequency if the delay does not equal the dither quarter-period, $T_d/4$, i.e., to reduce δT_e to zero value. The error signal ΔV_e is added to the voltage supplied to the PZT of the laser.

function generator, which serves as a master clock, is added to the output of the servo DAC and the voltage sum, V, is applied to the PZT of the diode laser to control its frequency. The sawtooth waveform signal (blue) applied to the PZT, shown in trace (a) results in the periodic sweeping (dither) of the laser frequency around the CRDS cavity resonance (shown to the left of the trace (a) in red). Ideally, the center frequency of the sweep coincides with the cavity resonance frequency resulting in the equally-separated ring-down events, shown as green decay traces, occurring twice a period. Under such circumstances, the ring-down events occur at $T_d/4$ and $3T_d/4$ times since the frequency sweep reversal, which is marked by the function generator sync signal, shown in trace (b).

The ring-down events are initiated when the signal on the photodiode generated by the light injected into the cavity by the laser in resonance reaches a pre-set value. This causes the delay generator to decouple the laser beam from the cavity by switching off the AOM and to issue a digital signal as shown in trace (c) of Fig. 6 which is recorded by the ADC for future data processing. Both digital signals (shown in panels (b) and (c)) are interfaced through the parallel port to the servo computer where the real-time software measures delay between them. When the dither center frequency drifts away from the cavity resonance, the delay between sync signal and ringdown event changes. This change, δT_e, is used to generate the analog error signal which is added to the DC offset of the analog signal supplied to the PZT of the laser such that the center dither frequency is restored to the cavity resonance. Such a correction is performed once a period. If the error signal reaches the limit of the DAC range, the DAC voltage is rolled back to match the frequency of the adjacent cavity resonance. The addition of the analog signals from the function and error signal from DAC is performed by a mixing circuit MX (see Fig. 3) in which the function generator output is attenuated by a factor of 4, and the DAC output is attenuated by a factor of 10 to reduce the effect of the digital noises from the DAC and increase the flexibility in adjustment of the dither amplitude. This pseudo-locking protocol is capable of maintaining the frequency following for as long as 20 continuous minutes with a frequency dither amplitude of about 30 MHz.

The data are taken in frames as illustrated in Fig. 7. The data frame is a segment of the continuously acquired data of typically 150 ms duration. Trace (a) shows the sawtooth signal described above, which results in the succession of the ringdown events schematically shown as vertical bars in trace (b). The analysis of the decay time constant of each ring-down event produces a single data point on the absorption plot. Such data points are shown as circles in trace (c). The trigger for the ADC installed in the control computer (see Fig. 3) to start acquisition is supplied by the real-time program run by the servo computer at $t = 0$ mark, as shown on trace (d). The first portion, between 0 and 50 ms of the data frame, occurring before the photolysis laser fires, is used to collect the baseline information. At the 50 ms mark, a trigger pulse is issued to fire the photolysis laser to initiate chemical reaction leading to the formation of the peroxy radicals and their subsequent decay. The second portion of the data frame, 100 ms long, is dedicated toward acquiring the kinetic decay data. Each data frame record contains 500–600 ringdown events, which are used to generate a single kinetic decay curve, as shown in trace (c). The repetition rate of the data frames is adjusted according to the pumping speed of the reaction cell to allow for complete refreshment of the sample between two successive photolysis events, as will be discussed below. A succession of 100–250 data frames taken under the identical conditions is stored in a single file whose size is limited by the file system of the control computer where the data are stored. Large continuous amounts of data are generated by running a data acquisition device in the “streaming” regime. In this regime, the on-board memory buffer is used as a pipe, which continuously transfers the incoming data into the hard drive. To avoid overrunning the on-board memory buffer, the data acquisition rate (16 MB/s) should be slower than the SATA data transfer rate (300 MB/s for SATA 2.0). This condition is readily achieved. Due to the large data input rate, the raw data are not processed in real time but stored in the computer and are processed (and, if necessary, re-processed) later.

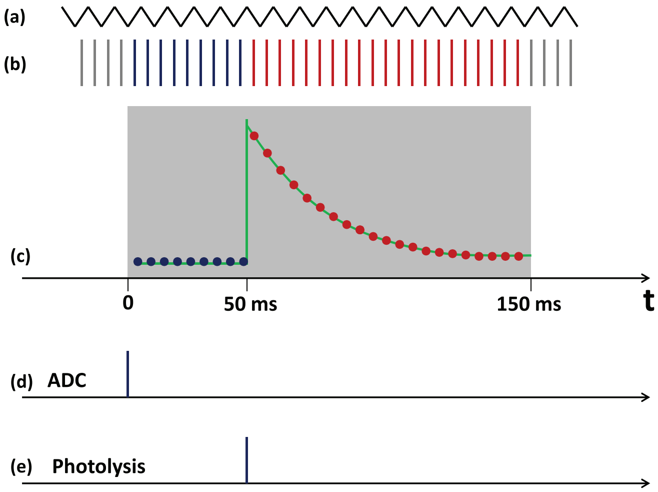

FIG. 7. The structure of the data frame. Panel (a) shows periodically swept voltage supplied to the ECDL, resulting in the succession of the ring-down events (panel (b)). A 150 ms duration of the raw signal is recorded by the ADC (shaded area in panel (c)) after a trigger pulse (panel (d)) is issued by a servo computer. The raw ring-down curves are processed to obtain a single absorption data point (dots on the curve in panel (c)) per ring-down event. The data obtained during the first 50 μs (blue dots) prior to triggering the photolysis laser (panel (e)) are used to calculate the baseline for radical absorption, the rest of the data (red dots) are used to derive kinetic rate constant.

C. Experimental parameters and conditions

For the kinetic experiments, the ethyl peroxy radicals were generated by the 193.3 nm photolysis of a gas mixture consisting of dry air and 3-pentanone vapor. The photolysis of 3-pentanone produces two ethyl radicals,[49] see Eq. (1a), followed by the formation of the ethyl peroxy radicals and subsequent reactions as described by Eqs. (1a)–(11). The precursor mixture is prepared in a gas manifold consisting of three separate lines. Dry air is supplied through a 2000 sccm (standard cubic centimeters per minute) MKS flow controller which forms the main line. The organic precursor

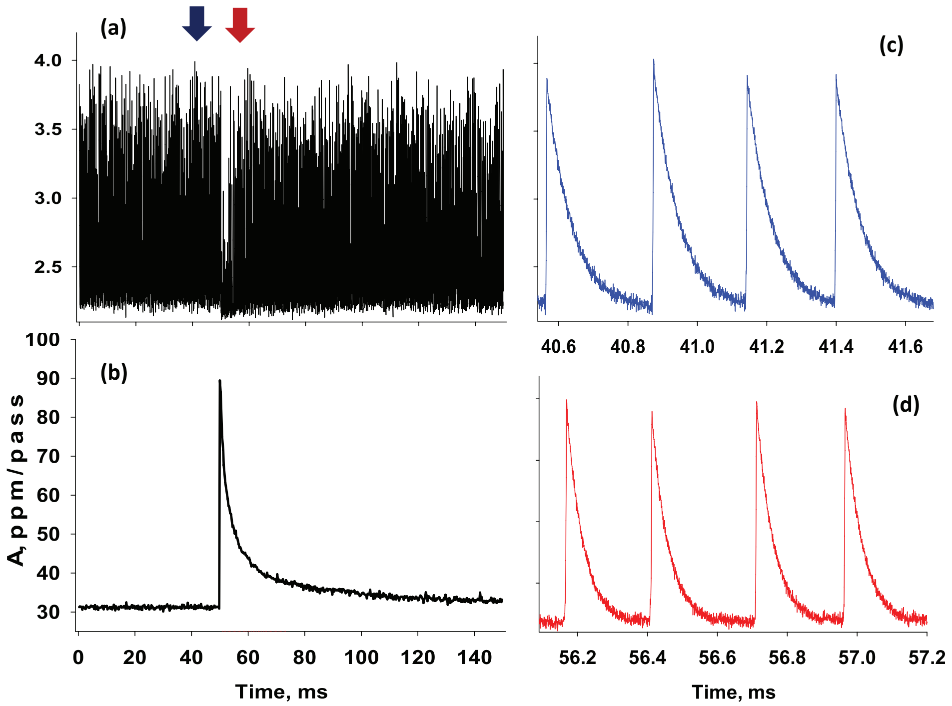

FIG. 8. The details of the experimentally observed ring-down and kinetic decays. Panel (a) shows the raw signal containing ≈540 ring-down decay curves. Panel (b) shows the kinetic decay curve determined from the ring-down decay traces, and plotted on the same time scale as panel (a). Panels (c) and (d) show expanded portions of the raw data containing 4 ring-down curves without and with radicals present at times marked with blue and red arrows in panel (a), respectively. The shaded portion in panel (b) shows the region of the decay curve that was used to determine the rate constant.

component is prepared by slow bubbling of the dry air though liquid 3-pentanone kept at room temperature and is supplied by a line through the 50 sccm flow controller. The third line (100 sccm, dry air) is used to form a protective curtain for the ringdown mirrors. Dry air in all three lines is supplied by a common gas cylinder. The experiments are conducted at ambient temperature 298(1) K in a temperature-stabilized environment, at a total pressure of 300 Torr, i.e., the same conditions that were used in the measurements of the peak absorption cross-section in the preceding work.[33] The number density of 3-pentanone was varied in the range of 0.6–1.8 $\times$ 10^{16} cm $^{-3}$. The flow conditions are adjusted by throttling the pump. The total gas flow rate was varied in the range of 70-165 sccm. Ethyl peroxy radicals were probed at the peak absorption frequency of the G-conformer of ethyl peroxy radical[33] at 7596 cm^{-1}.

For measurements of the effective flow speed, u, at the sample axis, we monitored absorption of t-butyl peroxy[50] whose self-reaction rate constant[4] at 298 K is $k_{obs}^{t-b} = 3 \times 10^{-17}$ cm^3/s. Its half live under typical conditions, $N_0 \approx 10^{15}$ cm^{-3} is over 10 s. Hence for the purpose of our measurements on the time scale of ≈100 ms it can be considered chemically inert. To produce the sample of the t-butyl peroxy radicals, we use 2-bromo-2-methylpropane. The absorption of the t-butyl peroxy radicals was monitored at the frequency[50] of the $\tilde{A} \leftarrow \tilde{X}$ origin band at 7757 cm^{-1}. Additionally, similar measurements were performed by monitoring the time evolution of the reported[50] stable byproduct of the photolysis of 2-bromo-2-methylpropane at 7612 cm^{-1}. These complementary measurements are useful since the typical absorption signal at the origin of t-butyl peroxy is rather weak. Additionally, absorption measurements at 7612 cm^{-1} allowed us to check for possible 3-pentanone contamination of the gas lines before introducing the precursor for the t-butyl peroxy radical.

IV. RESULTS AND DISCUSSION

An example of the experimental results obtained for the kinetic decay of ethyl peroxy radicals is shown in Fig. 8. Panel (a) contains continuously acquired data containing approximately 540 ring-down decay curves with an average separation of 275 μs over the span of 150 ms. These ring-down events are used to derive the absorption data plotted versus time, $A(t)$, on panel (b) below on the same time scale. The portion of the raw and the corresponding absorption data preceding the 50 ms mark correlate with the ring-down events shown in blue in Figs. 7(b) and 7(c), respectively. These data are used to establish the absorption signal baseline and ensure the complete replenishment of the sample before the next photolysis laser pulse. It should be noted that in an earlier work[33] a baseline correction was applied to the spectrum of ethyl peroxy to remove the spectral interference due to an unidentified long-lived by-product. In the present experiment, a different chemical protocol was used. No evidence of deviation of the decay curve from the second-order law has been observed; hence no baseline correction has been introduced.

The portion of the trace in Figs. 8(a)–8(b) following the photolysis laser pulse at the 50 ms mark shows the ringdown events and corresponding absorption data which are schematically shown in red in Figs. 7(b) and 7(c). The portion of the kinetic decay curve in the time interval 1–26 ms after the photolysis pulse (i.e., 51–76 ms marks on the absolute scale and shown in Fig. 8(b) as shaded area) is used to derive the RRC of the ethyl peroxy radicals. An expanded view of the raw data showing a succession of ring-down events during the baseline and kinetic decay portion of the data frame are shown in panels (c) and (d), respectively.

As Eq. (18) indicates, beside the experimentally measured absorption decay function, $A(t)$, used to calculate the k_{obs}/σ_P for the ethyl peroxy under the conditions of the experiment, it is also necessary to obtain the values of L_0 and u. The former value is defined by the dimension of the laser photolysis beam along the line of sight. The effective flow rate, u, Eq. (17) is determined by monitoring the evolution of the absorption of the spectral features at 7757 cm^{-1} and 7612 cm^{-1} in the spectra of the chemically inert *t*-butyl peroxy radical. Due to the weakness of the signal, longer portions of the decay curve, 90 ms long, were used to determine the flow conditions. A typical experimental trace at 7612 cm^{-1} is shown in Fig. 9. The 10 ms fragment of the curve immediately following the photolysis pulse is excluded from the analysis to avoid the systematic effects due to transient processes, e.g., possible reactions with the methyl peroxy radicals that are formed as by-product of *t*-butyl peroxy synthesis.[50] The effect of the methyl peroxy byproduct on the decay curve of the ethyl peroxy is discussed in Appendix A.

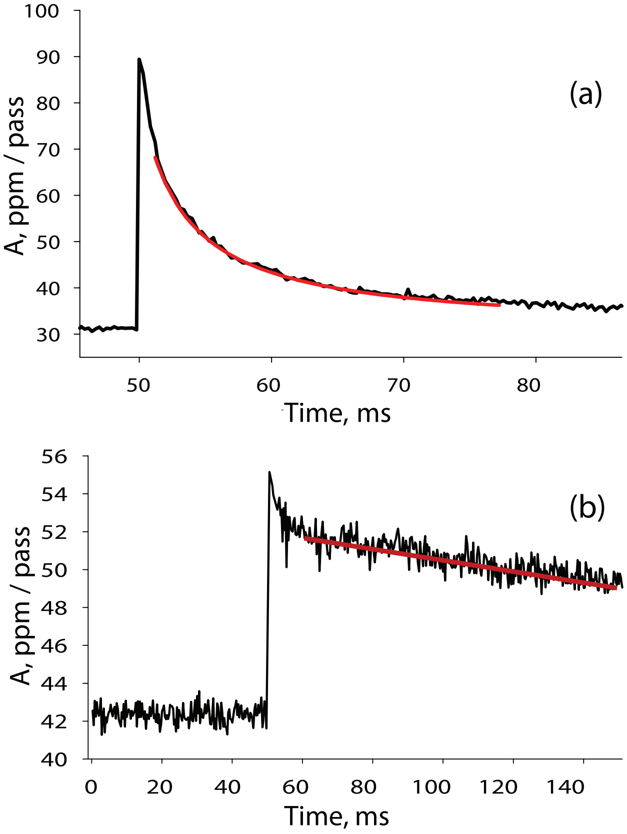

FIG. 9. Typical traces showing the evolution of the absorption of ethyl peroxy radicals at 7596 cm^{-1} (panel (a)) and inert species at 7612 cm^{-1} (panel (b)), taken at the flow rate of 70 sccm. Panel (a) shows an expanded view of the kinetic decay trace shown in Fig. 8(b). The shaded areas on both panels indicate the portion of the trace used for the determination of the effective flow rate. The red line shows the fit of the data to the corresponding absorption decay model (see text for details).

TABLE I. Experimental values of the effective flow rate, u, measured under two different flow conditions by observation of the absorption decay of the different features in the spectrum of the *t*-butyl peroxy radicals. The average effective rates, used for the kinetic data analysis at the corresponding conditions, $\bar{u}$ are shown in the last column.

Flow rate (sccm)	ν (cm^{-1})	u (cm/s)	$\bar{u}$ (cm/s)
70	7612	15(1)	15(1)
	7757	15(3)	
165	7612	18(2)	20(3)
	7757	22(2)	

Measurements were taken at two different flow conditions, 70 and 165 sccm total flow rates. In all experiments, the cell pressure was maintained at P = 300 ± 0.5 Torr. To measure the flow conditions, sequences of 50 data frames were obtained at both 7757 and 7612 cm^{-1} frequencies. The results of these measurements are shown in Table I. The values of the effective flow rate u obtained at different frequencies are consistent with each other at both flow conditions, therefore, the average values were used in the kinetic decay analysis. Although Eq. (18) allows us to use the experimentally measured value of u directly, we can make a rough estimate of flow velocity v at the axis of the sample and the first order diffusion loss rate, k_1. We assume that the flow velocity v for laminar isothermic flow is proportional to the total mass flow rate, and k_1 is invariant in all measurements since the pressure and temperature of the buffer gas is maintained at the same values. Solving Eq. (17) for two different conditions, we obtain $k_1 = 1.9$ s^{-1}, and the values of v for the slower and faster flow regimes used in these experiments at 3.7 and 8.7 cm/s, respectively. These estimates allow us to adjust the photolysis repetition rate such as to allow for full refreshment of the sample between the consecutive photolysis pulses. We estimate that the time required for the full sample refreshment, T_r is

$$T_r = \frac{2}{L_0} v, \tag{21}$$

where the factor of 2 accounts for non-uniformity of flow speed across the cell. This gives the values of T_r at 3.2 s and 1.4 s for the slower and faster regimes, respectively. The photolysis laser was fired every 5 s and every 3 s in the slower and faster flow regimes, respectively.

To obtain the experimental values of the (k_{obs}/σ_P), a total of six series of measurements, each consisting of 100–250 kinetic events (one per data frame) at different flow conditions, were made. The results of these measurements are summarized in Table II. For the global analysis, the individual measurements of the (k_{obs}/σ_P) from all six series were combined. The resulting value of the (k_{obs}/σ_P) is given in the last line of the table. The statistical distribution of the values of (k_{obs}/σ_P) obtained from single kinetic measurements is given in Fig. 10. Combining this value with the previously obtained value of $\sigma_P = 5.29(20) \times 10^{-21}$ cm^2 for the $\tilde{A} \leftarrow \tilde{X}$ origin

TABLE II. Summary of the results for the kinetic decay of ethyl peroxy radicals. All uncertainties are 1 σ.

Series	Frames	$N_0 \times 10^{-15}$ (cm^{-1})	u (cm/s)	$\left(\frac{k_{obs}}{\sigma_P}\right)$ (10^7 cm/s)
1	250	1.29(7)	15(1)	1.82(3)
2	250	1.19(6)	15(1)	1.81(3)
3	100	0.88(4)	20(3)	1.82(5)
4	100	0.91(4)	20(3)	1.84(5)
5	250	0.85(4)	20(3)	1.86(5)
6	249	0.85(4)	20(3)	1.85(5)
Total	1199	…	…	1.827(45)

TABLE III. Summary of the experimental values reported for k_{obs} for the self-reaction of the ethyl peroxy radicals. All uncertainties are 1 σ.

k_{obs} (10^{-13} cm^3/s)	Reference
1.08(34)	Lightfoot *et al.*[2]
0.91(23)	Wallington *et al.*[4]
1.03(29)	Atkinson[5]
1.29(7)	Fenter *et al.*[24]
1.20(9)[a]	Noell *et al.*[25]
1.24(41)	Atkinson and Hudgens[26]
0.966(45)	**This work**

[a] Value obtained at P = 200 Torr, T = 295 K.

band of the G-conformer of the ethyl peroxy, we obtain

$$\left(\frac{k_{obs}}{\sigma_P}\right) = 1.827(45) \times 10^7 \text{ cm/s}, \tag{22a}$$

$$\sigma_P = 5.29(20) \times 10^{-21} \text{ cm}^2, \tag{22b}$$

$$k_{obs} = 9.66(44) \times 10^{-14} \text{ cm}^3/\text{s}, \tag{22c}$$

where the numbers in parentheses indicate 1σ for the statistical uncertainties. The value of the k_{obs} obtained in this work is compared to the values previously reported by various groups in Table III. It is consistent with the previously reported values except those by Fenter *et al.*[24] and Noel *et al.*[25] Table III shows that the precision of the present measurements is considerably greater than most of previous ones. Nonetheless, the accuracy of these measurements can potentially be affected by a number of unaccounted processes and approximations. In Appendix A, we examine some of these factors and show that an intelligent choice of the mathematical model and experimental conditions can reduce systematic errors to values comparable to the statistical errors.

V. SUMMARY

In the this work, we have demonstrated an extension of the dual-wavelength CRDS apparatus reported previously[33] which was used to measure the absolute absorption cross-section, σ_P, of the reactive species. This extension permits the accurate measurement of the reaction RRC using time-resolved CW-CRDS spectroscopy. This apparatus has a high duty factor which allows for the determination of the absorption decay rates, (k_{obs}/σ_P), with high precision, and allows for the dimensions of the reaction region and the volume of the reactive sample to be substantially smaller than those typically used for kinetic measurements. An error analysis indicates that the systematic errors should be relatively small and comparable with the statistical uncertainties of the measured k_{obs}.

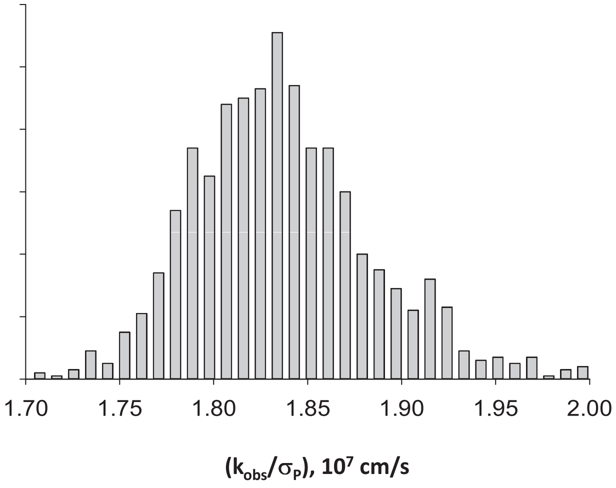

FIG. 10. Statistical distribution of the values of (k_{obs}/σ_P) obtained from individual measurements in the combined data set.

To illustrate the capability of the apparatus, we have measured the effective self-reaction rate of ethyl peroxy radicals by monitoring the evolution of the absorption at the peak of the $\tilde{A} \leftarrow \tilde{X}$ origin band of the G-conformer of this molecules. The experimentally measured absorption decay rate, (k_{obs}/σ_P), and previously measured value of the peak absorption cross-section were used to derive the value,

$$k_{obs} = 9.66(44) \times 10^{-14} \text{ cm}^3/\text{s}$$

at room temperature. This reported value of k_{obs} is consistent with the majority of the previously reported values of this quantity; however, it enjoys lower experimental uncertainties and is likely less time consuming to obtain than previously reported measurements.

We have demonstrated that the presented experimental setup is capable of performing accurate and precise measurements of the RRC and peak absorption cross-sections in complementary but independent experiments, resolving the correlation between these parameters, often present in earlier measurements. The present version of this apparatus can be used for measurement of the (k_{obs}/σ_P) within a dynamic range of nearly two orders of magnitude without any further modification.

ACKNOWLEDGMENTS

We would like to thank Adib Samin and Dr. Alexander Kachanov for the discussion and general help. This work is supported by the U.S. Department of Energy (DOE), Grant No. DE-FG-02-01ER14172.

APPENDIX A: ERROR ANALYSIS

To evaluate the precision and accuracy of the measurements of k_{obs} it is important to discuss various sources of errors in these measurements and their impact on the final result.

1. Statistical errors

The statistical uncertainty of k_{obs} in Eq. (22c) receives contributions from two major sources as it is calculated from the two independently measured values. For the distribution of the individual measurements of (k_{obs}/σ_P) shown in Fig. 10 the statistical uncertainty is given in Eq. (22a). Its half-width corresponds to a statistical error of 2.5%. This uncertainty is due to a modest signal-to-noise ratio for the individual ringdown traces. The noise in the ringdown curve results in random fluctuations of the calculated absorption which propagate to random noise for the derived value of (k_{obs}/σ_P). This error sets the limit of the precision for the measurements of the RRC using the present apparatus. The second source of the statistical error is the experimental uncertainty for σ_P, which is about 4.1%, and whose analysis is given in Ref. 33. Under these conditions the actual precision of 4.6% is practically limited by the σ_P measurement.

a. Errors in the effective flow rate measurements

An additional contribution to the random error which needs to be explicitly considered results from the error propagation from the experimental uncertainty in u, which can affect the derived value of (k_{obs}/σ_P). As seen in Fig. 9, the signal-to-noise ratio for the absorption decay traces of "quasi-stable" species which were used for measurement of the effective flow rate, is rather poor, which resulted in the uncertainties of the experimental values of u (see Table I). The apparent solution to this problem is to use a longer period of the experimental trace for the numerical analysis. On the other hand, these measurements should be done over a period of time which is short enough to approximate the absorption decay of the inert species by a linear law, Eq. (16). We found that the optimum range for the data analysis is within 10–100 ms after the photolysis pulse. At longer times, the decay curve exhibits non-negligible nonlinear character due to the exponential factor in Eq. (15), which would lead to underestimation of the value of u if the decay trace is fit to the linear law. At times shorter than 10 ms, a faster kinetic decay of the spectrum carrier is observed, possibly due to the reaction with the trace amounts of the methyl peroxy radicals that are also generated as a by-product of the *t*-butyl peroxy synthesis.[50]

The inclusion of the macroscopic and diffusional removal in the analysis of the kinetic decay of the ethyl peroxy radicals partially accounts for the removal of the reactive species from the sample, hence u is expected to negatively correlate with the k_{obs}/σ_P. We performed several model runs of the fit of the kinetic decay data with varying preset values of u and obtained the value of the correlation factor,

$$\partial\left(\frac{k_{obs}}{\sigma_P}\right)\Big/\partial u \approx -6\times 10^{4}, \tag{A1}$$

which implies that 3 cm/s uncertainty of the experimental value of u propagates into 2×10^5 cm/s contribution to the uncertainty of the k_{obs}/σ_P, which is small compared to 1σ of distribution shown in Fig. 10. Since the experimentally measured values of u are randomly distributed, the uncertainty in u contributes to random rather than systematic errors.

2. Systematic errors

a. Implications of reactions, Eqs. (1h)–(1l), for the observed decay process

The analysis in the present paper is based on the assumption that the observed removal of the ethyl peroxy radicals obeys a second order kinetic decay law, Eq. (4), with the effective rate constant, k_{obs} which is related to the rate constants of the elementary processes, e.g., as shown in Eq. (2). This relationship holds as long as secondary chemical processes following reaction, Eq. (1d), result in rapid stoichiometric removal of two additional peroxy radicals. While the competing reactions, Eqs. (1h)–(1l), do not necessarily alter the form of the decay law, they will affect the relationship, Eq. (2). While the present studies are not aimed at elucidating the latter relationship, it is still useful to estimate the impact of the competing reactions on the value of the k_{obs}.

To do that we performed a series of quantitative calculations of the temporal profile of the reactive species at the conditions of the experiment ($N_{C_2H_5} = 10^{15}$ cm^{-3}, T = 298 K, P(air) = 300 Torr) using the complete reaction mechanism in Eq. (1), such as those shown in Fig. 1. The calculated temporal profile of ethyl peroxy radicals obtained from these detailed calculations were subsequently fit to the simple second order decay function, Eq. (4). This procedure has been repeated while the value of the effective self-reaction rate constant for HO$_2$, $k^{eff}_{HO_2} = k_{1h} + k_{1i}N_{N_2} + k_{1j}N_{O_2}$ has been varied while all other RRCs were fixed. Similar calculations have been performed for the reactions, Eqs. (1k) and (1l). The partial derivatives of the k_{obs} with respect to $k^{eff}_{HO_2}$ and k_{1k} were obtained

$$\left(\frac{\partial k_{obs}}{\partial k^{eff}_{HO_2}}\right)_{k^{eff}_{HO_2}=2.05\times 10^{-12}} = -5.8\times 10^{-5}, \tag{A2}$$

$$\left(\frac{\partial k_{obs}}{\partial k_{1k}}\right)_{k_{1k}=1.7\times 10^{-11}} = -6\times 10^{-6}, \tag{A3}$$

$$\left(\frac{\partial k_{obs}}{\partial k_{1l}}\right)_{k_{1k}=1.7\times 10^{-11}} = -1.1\times 10^{-5}. \tag{A4}$$

Overall, the variation of $k^{eff}_{HO_2}$ within two orders of magnitude, from 1×10^{-13} to 1×10^{-11} resulted in about 0.5% variation of the calculated value of k_{obs}. Similar results (0.3%) was obtained for the variation of the k_{1k} within two orders of magnitude, from 2×10^{-12} to 2×10^{-10} and for k_{1l} (1.5%) for variation of the latter from 1.6×10^{-12} to 1.6×10^{-10} cm^3/s. Therefore, we conclude that the effect of reactions, Eqs. (1h)–(1l), on the overall ethyl peroxy decay rate at the conditions of the experiment, and the propagation of the uncertainties for the corresponding RRCs are negligible.

b. Presence of other reactions

The number density of the ethyl peroxy radicals can be straightforwardly measured from the absorption at $t = 0$, the length of the sample, L_0, and the peak absorption cross-section, σ_P, using Beer's law. The decay curves, such as shown in Fig. 8(b), are analyzed under the assumption of the reaction mechanism of Eq. (1). If other reactive species are generated by the photolysis and subsequent chemistry, the decay of the ethyl peroxy radicals may no longer be described by Eq. (1). An example of such an independent decay process can be seen in Fig. 9 within a few 10 ms after the photolysis pulse. The two most likely reactive by-products are C_2H_5CO (or its derivatives) and CH_3O_2. Although the formation of the acyl radicals from the photolysis of ketones is possible at longer photolysis radiation wavelengths,[51] the photon energy at 193.3 nm allows for the direct formation of two alkyl radicals.[52] No detectable trace of acyl byproducts[49] are experimentally observed hence it is unlikely that C_2H_5CO contributes to the chemistry.

However, small amounts of methyl peroxy radicals were detected in the *t*-butyl peroxy[50] and ethyl peroxy spectra.[31] At $t = 0$, their reaction with the ethyl peroxy contributes to the rate of removal of the latter by $-k_{12}N_0N_0^{MP}$, where k_{12} is the observed reaction rate between the ethyl and methyl peroxy radicals and N_0^{MP} is the initial concentration of methyl peroxy. The initial concentration of the CH_3O_2 radicals can be estimated from the survey scan traces over the spectrum range of ethyl peroxy radicals[31] and the reported value[30] of its peak absorption cross-section $\sigma_P^{MP} = 2.7\times10^{-20}$ cm^2. The amplitude of the feature identified as the origin of the CH_3O_2 by Rupper *et al.*[31] is about 5% of the amplitude of the origin of the G-conformer of the ethyl peroxy. Since σ_P^{MP} is nearly 5 times larger than σ_P, we deduce that the initial concentration of the methyl peroxy is two orders of magnitude smaller than that of the ethyl peroxy radicals.

The reported value[5,37,53] of the $k_{12} = 2\times10^{-13}$ cm^3/s is comparable with k_{obs}, hence at the conditions of the experiment, the main mechanism for the removal of methyl peroxy radicals from the reaction region is its reaction with ethyl peroxy radicals. For the purpose of rough estimate we can assume that the temporal profiles of the two radicals are similar, and obtain an estimate of the systematic error due to the cross-reaction between two species

$$\delta k_{obs} = -k_{12}\frac{N_0^{MP}}{2N_0} \approx -10^{-15}\ \mathrm{cm^3/s}, \tag{A5}$$

which constitutes about 1% overestimate of the k_{obs}.

c. Longitudinal spatial non-uniformity of the reactive sample

Equation (10) was obtained under the assumption that the reactive sample is spatially uniform, so that $N(x, t)$ factors out from the integration over the beam path. In reality, the sample has some non-uniformity, and the distribution of the number density, $N(x, 0)$, maps from that of the photolysis beam intensity $I_p(x)$. To maximize the uniformity of the sample, we used a mask which blocks lateral, low-intensity parts of the photolysis laser beam, creating a rectangular sample 6 cm long and 8 mm tall, along the axis of the probe beam. The photolysis beam intensity distribution within the open region was measured using a smaller, 5 mm long mask which could sample the beam at the desired value of x. The results of these measurements are shown in Fig. 11.

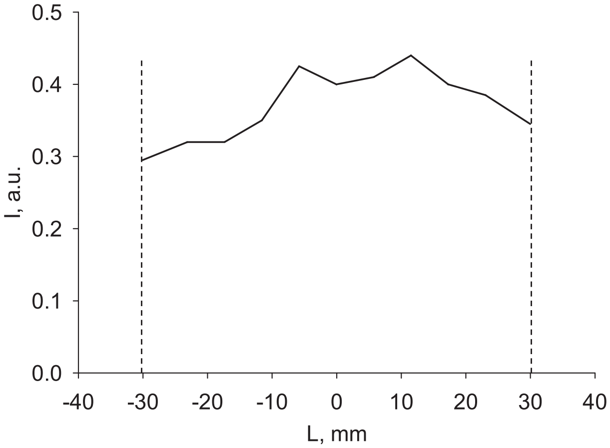

FIG. 11. The spatial distribution of the intensity, in arbitrary units, of the photolysis laser beam along the axis of the sample relative to its midpoint.

To estimate the errors due to the observed sample non-uniformity we assume that during the time interval of the kinetic measurements (25 ms) the sample length remains essentially unchanged. We also assume that the spatial variation of the sample density is relatively small, and express $N(x, 0)$ as a weakly varying function of x with an average value, N_0. Its spatial variation is described by a dimensionless function $f(x)$, whose integral over the optical path vanishes, in accordance with the definition of the N_0, Eq. (10b):

$$N(x, 0) = N_0\,(1 + f(x))\,, \tag{A6a}$$

$$\int_0^{L_0} f(x)dx = 0, \tag{A6b}$$

and N_0 is defined in Eq. (10b), and $f(x)$ is a dimensionless distribution function. Expanding the exponentials in Eq. (8) and substituting the results, along with Eq. (A6) into Eq. (9), we obtain

$$A(t) = \sigma_P\,(1 - k_1 t)\int_0^{L_0 - vt}\frac{N_0(1 + f(x))}{1 + 2k_{obs}N_0 t} \times \left(1 - \frac{2k_{obs}N_0 f(x)t}{1 + 2k_0N_0t}\right)dx. \tag{A7}$$

In the expression under the integral, $f(x)$ is the only coordinate-dependent quantity. Since its integral over L_0 vanishes, we rewrite Eq. (A7), ignoring small terms quadratic in t, as

$$A(t) = \frac{(1-k_1 t)\,A_0\left[1-\dfrac{v}{L_0}t\right]}{1+2\left(\dfrac{k_{obs}}{\sigma_P}\right)\dfrac{A_0}{L_0}} \times\left\{1-\frac{1}{L_0}\frac{2k_{obs}N_0 t}{1+2k_{obs}N_0 t}\int_0^{L_0} f^2(x)dx\right\}. \quad \text{(A8)}$$

The fraction in front of the curly brackets on the right hand side of Eq. (A8) reduces to the right hand side of Eq. (18). The integral within the curly brackets on the right-hand side is related to the variance of the radical number density, χ_N^2 which we assume is the same as the variance of the photolysis beam intensity shown in Fig. 11,

$$\chi_N^2 = \frac{1}{L_0}\int_0^{L_0} f(x)^2 dx. \quad \text{(A9)}$$

We now show that the sample nonuniformity affects the measured value of k_{obs} directly, i.e., it contributes to the second order term in Eq. (7) by addition of the systematic error $\delta_n k_{obs}$. Substituting $k_{obs} + \delta_n k_{obs}$ for the k_{obs} in Eq. (10a) and performing the expansion of the exponentials and rearranging the terms as we did for Eq. (A7), we obtain

$$A(t) = \frac{(1-k_1 t)\,A_0\left[1-\dfrac{v}{L_0}t\right]}{1+2\left(\dfrac{k_{obs}}{\sigma_P}\right)\dfrac{A_0}{L_0}}\left\{1-\frac{2\delta_n k_{obs}N_0 t}{1+2k_{obs}N_0 t}\right\}. \quad \text{(A10)}$$

Comparing Eqs. (A8) and (A10), we find the value for the systematic error due to the sample nonuniformity,

$$\delta_n k_{obs} = k_{obs}\chi_N^2. \quad \text{(A11)}$$

For the beam intensity distribution shown in Fig. 11 we find $\chi_N^2 = 0.017$, hence the corresponding sample nonuniformity results in the overestimate of the k_{obs} by 1.7%.

In addition to bulk sample non-uniformity, two other effects need to be discussed. First, it is the effect of the radical diffusion along the sample axis. This effect will be most prominent at the ends of the sample where the gradient of radical concentration will be the greatest. This gradient will cause the radicals to diffuse outwards, creating regions where the sample concentration will be lower than in the middle of the sample and simultaneously extending the overall sample length. While the total absorption within the sample will be unaffected by this process, radicals in the region with reduced concentration at the ends of the sample will decay slower, resulting in underestimation of k_{obs}/σ_P. Similar processes in the middle of a nonuniform sample result in transfer of radicals from more dense to less dense regions and are expected to mediate the effects of the spatial sample nonuniformity discussed above. Hence, we will discuss only the systematic error due to diffusion effects at the ends of the sample. Such systematic error can be estimated by the degree of the sample extension by $t = \tau_{1/2}$ due to diffusion. This extension is characterized by the mean-squared displacement of the radical at the sample border,

$$\langle x^2\rangle = 2D\tau_{1/2}, \quad \text{(A12)}$$

where D is the diffusion coefficient for ethyl peroxy radical in air. A diffusion coefficient of ethyl peroxy radicals is not available, therefore for the purpose of estimate we use the value of D for ethanol provided by the EPA.[54] For the conditions of the experiment (T = 298 K, P= 300 Torr), $D = 0.316$ cm^2/s, therefore the overall sample extension, δL can be found at

$$\delta L = 2\sqrt{\langle x^2\rangle} \approx 1.8 \text{ mm}. \quad \text{(A13)}$$

The factor of 2 is introduced to account for both ends of the sample. This constitutes 3% of the sample length, and is expected to translate into the corresponding value of systematic error for k_{obs}/σ_P.

Finally, we take into account "leaking" of the excimer radiation outside of the mask, thus creating an uncertainty in the actual sample length. The photolysis beam from the excimer laser entering the cell is reshaped by two lenses, cylindrical, and spherical. This arrangement creates a beam focus, less than 1 mm wide, in the plane of the probe IR beam at the distance 60 cm from the sample axis. The mask is placed 20 cm away from the sample axis, thus the expected uncertainty of the sample length is about 0.33 mm at each side, which is about 1% of the sample length.

d. Transverse spatial sample nonuniformity

To use Eq. (7) instead of Eq. (6) we assumed that the diffusion term in the latter equation can be replaced with the first-order kinetic term in the former equation. To test this assumption we assume that the chemical removal of radicals occurs at a much greater rate than the physical removal due to diffusion. Therefore, we need to find conditions under which the diffusion in the direction perpendicular to the sample axis exhibits the same behavior as the first order kinetic term, i.e., its value is proportional to $N(t)$. To do that we consider a spatial distribution of radicals which is non-uniform along the axis y, perpendicular the line of sight, and whose initial distribution follows the one-dimensional Gaussian profile of the photolysis laser,

$$N(y, t=0) = N_0 \exp\left[-\left(\frac{y}{y_0}\right)^2\right], \quad \text{(A14)}$$

where y_0 is the half-width of the photolysis laser beam in the direction perpendicular to the probe laser beam. Since we assume that the sample is uniform along the other two directions, then the diffusion term at the axis of the sample is written as

$$D\nabla^2 N(0, t=0) = \lim_{y\to 0} D\frac{\partial^2}{\partial y^2}N(y, t=0) = -\frac{2DN_0}{y_0^2}, \quad \text{(A15)}$$

which means that at $t = 0$ the condition is fulfilled, and comparison of Eqs. (6) and (7) and (A15) gives $k_1 = 2D/y_0^2$. To obtain an expression for this term at times other than $t = 0$, we substitute the expression in Eq. (A14) into Eq. (4) and evaluate $\lim_{y\to 0} D\nabla^2 N(y, t)$ as a function of time. We obtain, explicitly removing coordinate dependence,

$$D\nabla^2 N(t) = -\frac{2DN_0}{y_0^2\left(1+2k_{obs}N_0 t\right)^2} = -\frac{2DN(t)}{y_0^2\left(1+\frac{t}{\tau_{1/2}}\right)}, \tag{A16}$$

where the half-life time $\tau_{1/2}$ is given by Eq. (19). In notation of Eq. (7), the k_1 constant becomes time-dependent,

$$k_1(t) = \frac{2D}{y_0^2\left(1+\frac{t}{\tau_{1/2}}\right)}. \tag{A17}$$

We see that Eq. (7) is approximately valid at times $t < \tau_{1/2}$. For t-butyl peroxy, it remains valid during all the measurement period (≈90 ms), since for these species $\tau_{1/2}$ is over 10 s. However, for the ethyl peroxy, measurements are carried out for a period exceeding $\tau_{1/2}$ by an order of magnitude, over which the impact of diffusion greatly diminishes. Therefore, the use of the value of u obtained from the t-butyl peroxy for the analysis of kinetic decay of ethyl peroxy will result in a systematic error in the measured value of k_{obs}/σ_P. The magnitude of this error can be estimated as follows. At $t < \tau_{1/2}$ the impact of this error is negligible, and gradually grows to its largest value towards the end of the measurement. Diffusion provides a major contribution to the value of u, e.g., for t-butyl peroxy $k_1 L_0 \approx 12$ cm/s (see discussion below), we can estimate the overall systematic error due to treatment of k_1 as constant for the measurements of the ethyl peroxy kinetic decay over the period of $10\tau_{1/2}$ as

$$0.76 \cdot k_1 L_0 \partial\left(\frac{k_{obs}}{\sigma_P}\right)\Big/\partial u = -5.4\times\ 10^5\text{cm/s}, \tag{A18}$$

where the factor 0.76 is $1-\overline{k_1(t)}/k_1(0)$, and the numerical value for the partial derivative from Eq. (A1) is used. This systematic error is comparable in magnitude to the random errors in Eq. (22a) and results in an underestimate of the k_{obs}/σ_P as it results from radical loss to diffusion rather than to kinetic decay.

It is interesting to note that systematic errors due to reaction with methyl peroxy radicals and longitudinal nonuniformity on the one hand, and oversimplification of the physical kinetic processes on the other hand, result in the systematic errors that have opposite but comparable effects on the determined value for k_{obs}.

e. Other model approximations

Up to now we have used Eq. (18) as a solution of Eq. (7). This is a useful approximation which allows us to interpret the physical significance of the parameters k_1 and v (see Eq. (17)) and to apply the results of the flow rate measurement to the analysis of the kinetic decay. In doing that, however, we have made two assumptions.

First, we treated k_1 as a time-independent parameter and subsequently replaced the exponentials arising from the first-order term in Eq. (7) with its power series expansion truncated at the linear term. As shown in Fig. 2(b), such an assumption results in the overestimation of the effective flow rate (red curve) compared with the rigorous solution of Eq. (15). The choice of the parameters in these simulations arose from the comparison of the values of u at the different flow rates shown in Table I. Since an increase of the flow rate by a factor of 2.4 results only in a moderate increase of u of about 30%, the diffusion processes, accounted for by k_1, must play a substantial role. Assuming v is proportional to the macroscopic flow rate and k_1 is independent of it, we obtain values of $k_1 = 1.9$ s^{-1} and $v = 3.7$ cm/s at the lower flow rate. As Fig. 2(b) shows that the experimental values of u measured over 100 ms portion of the decay curve are about 10% overestimated, which results in roughly a 10^5 cm/s underestimate of the k_{obs}/σ_P, or 0.5% underestimate in the determination of k_{obs}.

Second, we assumed that the flow speed is low enough so that the flow is laminar and any turbulence effects can be ignored. The criterion for this flow type is defined by the value of the Reynolds number, Re[55]

$$Re = \frac{\rho v_m D_h}{\eta}, \tag{A19}$$

where ρ is the fluid (gas) density, v_m is the mean stream velocity, D_h is the hydraulic diameter of the cell, and η is the dynamic viscosity. For air at T = 295 K, the pressure-independent value of $\eta = 1.82\times10^{-5}$ kg m^{-1} s^{-1}, and the density of the air at P = 300 Torr is 0.51 kg m^{-3}. The mean stream velocity, v_m, for the isothermic flow at T = 298 K and pressure P can be estimated using an equation that is straightforwardly derived from the ideal gas law (i.e., assuming that the specific volume is inversely proportional to pressure),

$$v_m = \frac{V_{st}}{S_c}\frac{P_{st}}{P}, \tag{A20}$$

where V_{st} is the standard condition volumetric flow rate, given in the first column of Table I, $P_{st} = 760$ Torr, and S_c is the cell cross-section. Under the conditions of the experiment, the values of the v_m for the slower and faster flow regime are 1.0 and 2.4 cm/s, respectively, which are about 3 times smaller than the macroscopic flow speed, v, at the axis of the cell.

The hydraulic diameter of the pipe with the rectangular cross-section is given as

$$D_h = \frac{4S_c}{p_c}, \tag{A21}$$

where p_c is the perimeter of the cell cross-section. For the cell used in these experiments, $D_h = 1.67$ cm. Using the parameters of the expansion, we obtain values of the Reynolds number for the slower and faster flow regimes of 4.6 and 11.0, respectively. For fluid flow to be considered laminar, the value of the Reynolds number should stay[55] below 2300. Hence, turbulence effects at the axis of the cell can be ignored.

In summary, the combined systematic errors for the experimental measurements evaluated for the conditions of this work are of the order of the 2% of the reported value of k_{obs} which is comparable to the experimental uncertainties of the k_{obs}.

APPENDIX B: APPARATUS LIMITATIONS

It is worthwhile to consider the range of the absorption decay values, k_{obs}/σ_P which can be practically determined using the present experimental setup. To measure k_{obs}/σ_P

reliably, the following criteria must be met. First, the time resolution, Δt, must be sufficient to record M data points during $\tau_{1/2}$ period of time. Second, the signal-to-noise ratio of the absorption trace at $t = 0$ should be at least R_n^s, given the baseline noise level is A_n. Third, the maximum absorption amplitude at $t = 0$ should be at most A_M. The third criterion is imposed by the limited time resolution of the ADC that has to be sufficient to record the ring-down curve, and the stability issues of the frequency following scheme, described in the Experimental section.

Using these criteria, we first estimate the maximum measurable value of k_{obs}/σ_P. Summarizing the first two criteria, we obtain

$$M = \frac{\tau_{1/2}}{\Delta t} = \frac{1}{2N_0 k_{obs}\Delta t}, \tag{B1a}$$

$$R_n^s = \frac{L_0 \sigma_P N_0}{A_n}, \tag{B1b}$$

from which we derive

$$\left(\frac{k_{obs}}{\sigma_P}\right)_{max} = \frac{L_0}{2MR_n^s A_n \Delta t}. \tag{B2}$$

In the present experiments, $L_0 = 6$ cm, $A_n = 5 \times 10^{-7}$, $\Delta t = 2.5 \times 10^{-4}$, and we can specify the values of $M = 10$ and $R_n^s = 20$ using an order of magnitude argument. Using these values, we obtain

$$\left(\frac{k_{obs}}{\sigma_P}\right)_{max} \approx 10^8 \text{ cm/s}. \tag{B3}$$

To obtain the minimum measurable value of k_{obs}/σ_P we require that the chemical removal rate is much larger than the macroscopic and diffusion rate during at least $\tau_{1/2}$, i.e., at $t = 0$ it exceeds the physical removal rate by at least a factor of $R_r = 20$. Additionally, we require that the magnitude of the absorption at $t = 0$ does not exceed A_M. Therefore, we can write

$$2k_{obs}N_0^2 = R_r\left(k_1 + \frac{v}{L}\right)N_0. \tag{B4}$$

Using Beer's law for the A_M, we obtain

$$\left(\frac{k_{obs}}{\sigma}\right)_{min} = \frac{R_r}{A_M}(k_1 L_0 + v) = \frac{uR_r}{A_M}. \tag{B5}$$

For $A_M = 100$ ppm $= 10^{-4}$, and the limit of zero flow rate $u = L_0 k_1 \approx 10$ cm/s, we obtain

$$\left(\frac{k_{obs}}{\sigma}\right)_{min} = 2 \times 10^6 \text{ cm/s}. \tag{B6}$$

For measurements of slower rates, a larger cell, ensuring smaller values of k_1, could be implemented.

[1] S. W. Benson, Prog. Energy Combust. Sci. **7**, 125 (1981).

[2] P. D. Lightfoot, R. A. Cox, J. N. Crowley, M. Destriau, G. D. Hayman, M. E. Jenkin, G. K. Moortgat, and F. Zabel, Atmos. Environ. **26A**, 1805 (1992).

[3] S. Madronich and J. Calvert, J. Geophys. Res. **95**, 5697, doi:10.1029/JD095iD05p05697 (1990).

[4] T. J. Wallington, P. Dagaut, and M. J. Kurylo, Chem. Rev. **92**, 667 (1992).

[5] R. Atkinson, J. Phys. Chem. Ref. Data **26**, 215 (1997).

[6] G. J. Frost, G. B. Ellison, and V. Vaida, J. Phys. Chem. A **103**, 10169 (1999).

[7] T. J. Wallington and O. J. Nielsen, "Peroxy radicals and the atmosphere," in *Peroxyl Radicals* (John Wiley and Sons, New York, NY, 1997), p. 457.

[8] M. P. Fraser, D. Grosjean, E. Grosjean, R. A. Rasmussen, and G. R. Cass, Environ. Sci. Technol. **30**, 1731 (1996).

[9] X. Zhang, Z. M. Chen, S. Z. He, W. Hua, Y. Zhao, and J. L. Li, Atmos. Chem. Phys. **10**, 737 (2010).

[10] W. R. Stockwell, J. B. Milford, D. Gao, and Y.-J. Yang, Atmos. Environ. **29**, 1591 (1995).

[11] E. Villenave, R. Lesclaux, S. Seefeld, and W. R. Stockwell, J. Geophys. Res. **103**, 25273, doi:10.1029/98JD00926 (1998).

[12] S. H. Robertson, P. Seaking, and M. J. Pilling, *Low Temperature Combustion and Autoignition* (Elsevier, Amsterdam, 1997), Vol. 35, Chap. 1, p. XIII.

[13] H. J. Curran, P. Gaffuri, W. J. Pitz, and C. K. Westbrook, Combust. Flame **114**, 149 (1998).

[14] S. Wang, D. L. Miller, N. P. Cernansky, H. J. Curran, W. J. Pitz, and C. K. Westbrook, Combust. Flame **118**, 415 (1999).

[15] A. D'Anna, A. Violi, and A. D'Alessio, Combust. Flame **121**, 418 (2000).

[16] P. Biggs, C. Canosa-Mas, J. Francheboud, C. Percival, R. Wayne, and D. Shallcross, J. Chem. Soc., Faraday Trans. **93**, 379 (1997).

[17] G. S. Tyndall, R. A. Cox, C. Granier, R. Lesclaux, G. K. Moortgat, M. J. Pilling, A. R. Ravishankara, and T. J. Wallington, J. Geophys. Res. **106**, 12157, doi:10.1029/2000JD900746 (2001).

[18] H. Adachi, N. Basco, and D. G. L. James, Int. J. Chem. Kinet. **XI**, 1211 (1979).

[19] F. C. Cattell, J. Cavanagh, R. A. Cox, and M. E. Jenkin, J. Chem. Soc., Faraday Trans. 2 **82**, 1999 (1986).

[20] T. J. Wallington, P. Dagaut, and M. J. Kurylo, J. Photochem. Photobiol., A **42**, 173 (1988).

[21] D. Bauer, J. N. Crowley, and G. K. Moortgat, J. Photochem. Photobiol., A **65**, 329 (1992).

[22] C. Anastasi, D. J. Waddington, and A. Wooley, J. Chem. Soc. Faraday Trans. 1 **79**, 505 (1983).

[23] J. Munk, P. Ragsberg, E. Ratajczak, and A. Sillesen, J. Phys. Chem. **90**, 2752 (1986).

[24] F. F. Fenter, V. Catoire, R. Lesclaux, and P. D. Lightfoot, J. Phys. Chem. **97**, 3530 (1993).

[25] A. C. Noell, L. S. Alconcel, D. J. Robichaud, M. Okumura, and S. P. Sander, J. Phys. Chem. A **114**, 6983 (2010).

[26] D. B. Atkinson and J. W. Hudgens, J. Phys. Chem. A **101**, 3901 (1997).

[27] E. Villenave and R. Lesclaux, J. Phys. Chem. **100**, 14372 (1996).

[28] C. M. Roehl, D. Bauer, and G. K. Moortgat, J. Phys. Chem. **100**, 4038 (1996).

[29] H. E. Hunziker and H. R. Wendt, J. Chem. Phys. **64**, 3488 (1976).

[30] M. B. Pushkarsky, S. J. Zalyubovsky, and T. A. Miller, J. Chem. Phys. **112**, 10695 (2000).

[31] P. Rupper, E. N. Sharp, G. Tarczay, and T. A. Miller, J. Phys. Chem. A **111**, 832 (2007).

[32] E. N. Sharp, P. Rupper, and T. A. Miller, Phys. Chem. Chem. Phys. **10**, 3955 (2008).

[33] D. Melnik, R. Chhantyal-Pun, and T. A. Miller, J. Phys. Chem. A **114**, 11583 (2010).

[34] D. Melnik, P. S. Thomas, and T. A. Miller, J. Phys. Chem. A **115**, 13931 (2011).

[35] G. M. P. Just, A. B. McCoy, and T. A. Miller, J. Chem. Phys. **127**, 044310 (2007).

[36] S. J. Zalyubovsky, B. G. Glover, and T. A. Miller, J. Phys. Chem. A **107**, 7704 (2003).

[37] D. B. Atkinson and J. L. Spillman, J. Phys. Chem. A **106**, 8891 (2002).

[38] P. Zalicki and R. N. Zare, J. Chem. Phys. **102**, 2708 (1995).

[39] P. D. Lightfoot, P. Roussel, B. Veyret, and R. Lesclaux, J. Chem. Soc., Faraday Trans. **86**, 2927 (1990).

[40] J. Thiebaud, S. Crunaire, and C. Fittschen, J. Phys. Chem. A **111**, 6959 (2007).

[41] J. Thiebaud and C. Fittschen, Appl. Phys. B **85**, 383 (2006).

[42] M. J. Kurylo, P. Ouellette, and A. H. Laufer, J. Phys. Chem. **90**, 437 (1986).

[43] T. T. Paukert and H. S. Johnston, J. Chem. Phys. **56**, 2824 (1972).

[44] G. Moortgat, B. Veyret, and R. Lesclaux, J. Phys. Chem. **93**, 2362 (1989).

[45] P. S. Thomas, R. Chhantyal-Pun, and T. A. Miller, J. Phys. Chem. A **114**, 218 (2010).

[46] T. Stocker, *Introduction to Climate Modeling*, Advances in Geophysical and Environmental Mechanics and Mathematics (Springer, Berlin, 2011), p. 57.

[47] J. T. Hodges, J. P. Looney, and R. D. Zee, Appl. Opt. **35**, 4112 (1996).

[48] L. S. Rothman, I. E. Gordon, A. Barbe, D. Chris Benner, P. F. Bernath, M. Birk, V. Boudon, L. R. Brown, A. Campargue, J.-P. Champion, K. Chance, L. H. Coudert, V. Dana, V. M. Devi, S. Fally, J.-M. Flaud, R. R. Gamache, A. Goldman, D. Jacquemart, I. Kleiner, N. Lacome, W. J. Lafferty, J.-Y. Mandin, S. T. Massie, S. N. Mikhailenko, C. E. Miller, N. Moazzen-Ahmadi, O. V. Naumenko, A. V. Nikitin, J. Orphal, V. I. Perevalov, A. Perrin, A. Predoi-Cross, C. P. Rinsland, M. Rotger, M. Šimecková, M. A. H. Smith, K. Sung, S. A. Tashkun, J. Tennyson, R. A. Toth, A. C. Vandaele, and J. Vander Auwera, J. Quant. Spectrosc. Radiat. Transf. **110**, 533 (2009).

[49] J. Pola, Y. Koga, and A. Ouchi, Tetrahedron **53**, 3757 (1997).

[50] B. G. Glover and T. A. Miller, J. Phys. Chem. A **109**, 11191 (2005).

[51] B. Rajakumar, T. Gierczak, J. E. Flad, A. R. Ravishankara, and J. B. Burkholder, J. Photochem. Photobiol., A **199**, 336 (2008).

[52] G. E. Hall, H. W. Metzler, J. T. Muckerman, J. M. Preses, and R. E. Weston, J. Chem. Phys. **102**, 6660 (1995).

[53] D. Johnson, D. W. Price, and G. Marston, Atmos. Environ. **38**, 1447 (2004).

[54] See http://www.epa.gov/athens/learn2model/part-two/onsite/estdiffusion.html for EPA on-line tools for site assessment calculation.

[55] D. J. Hucknall and A. Morris, *Vacuum Technology: Calculations in Chemistry* (The Royal Society of Chemistry, Cambridge, UK, 2003).